Self-Templating Construction of 3D Hierarchical Macro-/Mesoporous Silicon from 0D Silica Nanoparticles

Xiuxia Zuo[1, 2], Yonggao Xia[1], Qing Ji[1, 3], Xiang Gao[4], Shanshan Yin[1, 5], Meimei Wang[1], Xiaoyan Wang[1], Bao Qiu[1], Anxiang Wei[1], Zaicheng Sun[4], Zhaoping Liu[1], Jin Zhu[1], and Ya-Jun Cheng[1, 6]

1. Ningbo Institute of Materials Technology & Engineering, Chinese Academy of Sciences, 1219 Zhongguan West Rd, Ningbo, 315201, Zhejiang Province, P. R. China

2. University of Chinese Academy of Sciences, 19A Yuquan Rd, Shijingshan District, Beijing, 100049, P. R. China

3. The University of Nottingham Ningbo China, 199 Taikang East Road, Ningbo, 315100, Zhejiang Province, P. R. China

4. Beijing Key Laboratory of Green Catalysis and Separation, Department of Chemistry and Chemical Engineering, School of Environmental and Energy, Beijing University of Technology, Beijing, P. R. China

5. North University of China, Shanglan Rd, Taiyuan, 030051, Shanxi Province, P. R. China

6. Department of Materials, University of Oxford, Parks Rd, OX1 3PH, Oxford, UK

E-mail address: chengyj@nimte.ac.cn

ABSTRACT: Porous silicon has found wide applications in many different fields including catalysis and lithium-ion batteries. Three-dimensional hierarchical macro-/mesoporous silicon is synthesized from zero-dimensional Stöber silica particles through a facile and scalable magnesiothermic reduction process. By systematic structure characterization of the macro-/mesoporous silicon, a self-templating mechanism

governing the formation of the porous silicon is proposed. Applications as lithium-ion battery anode and photocatalytic hydrogen evolution catalyst are demonstrated. It is found that the macro-/mesoporous silicon shows significantly improved cyclic and rate performance than the commercial nano-sized and μm-sized silicon particles. After 300 cycles at 0.2 A g^{-1}, the reversible specific capacity is still retained as much as 959 mAh g^{-1} with a high mass loading density of 1.4 mg cm^{-2}. With the large current density of 2 A g^{-1}, a reversible capacity of 632 mAh g^{-1} is exhibited. The coexistence of both macro and mesoporous structures are responsible for the enhanced performance. The macro-/mesoporous silicon also shows superior catalytic performance for photocatalytic hydrogen evolution compared to the silicon nanoparticles.

KEYWORDS: lithium-ion battery anode, porous silicon, self-templating, magnesiothermic reduction, macro-/mesoporous

Porous silicon plays a vital role in many different applications such as optoelectronics, lithium ion batteries, sensors and biomedical devices due to its unique structure feature and rich physical/chemical properties.[1-5] Particularly, Si has been identified as one of the most promising candidates for next-generation lithium-ion battery (LIB) anode because of its exceptional capacity, reasonable voltage output, and operation safety.[5-11] However, huge volume expansion upon lithiation causes series of adverse consequences, leading to poor cyclic stability.[5] Porous silicon can accommodate the drastic volume change and mitigate the corresponding mechanical stress. As a result, the major failure mechanisms responsible for rapid capacity fading can be inhibited, leading to enhanced cyclic performance.[12-14] Nevertheless, delicate structure design of the porous silicon is mandatory to achieve outstanding cyclic performance. Firstly, macropores are required within the porous silicon due to the huge volume change of more than 360 % upon lithiation. Secondly, mesopores are needed to provide sufficient surface area for electrolyte wetting, charge carrier transportation, and enhanced electrochemical kinetics. Therefore, the coexistence of both macro and mesopores are indispensable to improve the electrode structure stability, cyclic performance and enhanced electrochemical kinetics in a synergistic way. However, despite of the extensive research work on the porous silicon anode, there have been very limited studies on the synthesis, applications and fundamental structure-property correlation of the hierarchical macro-/mesoporous silicon.

The porous silicon is mainly synthesized by wet etching of silicon wafers,[15-18] chemical de-alloying,[19-21] and templating synthesis.[22] Nevertheless, these synthetic methods may need to use significant amount of toxic chemical (such as hydrofluoric acid), or expensive starting material (for example, silver). Particularly, the external template approach requires very sophisticated assembly process, which is very time consuming, tricky to control experimental parameters, and difficult to scale up.[23, 24] Compared to these methods, magnesiothermic reduction has emerged as an effective way to convert silica into silicon with precisely controlled microscale shapes and nanoscale features under relative mild condition in a facile

scalable way.[25-28] Decent amount of studies on the synthesis of the porous silicon by the magnesiothermic reduction have been published.[29-32] However, to our best knowledge, the coexistence of both macro and mesopores in the obtained silicon powders is quite rare. In a particular case, hierarchical porous silicon was synthesized through the magnesiothermic reduction reaction.[33] However, solid core/mesoporous shell SiO_2 spheres has to be used as the precursor, which is very tricky to synthesize. The synthesis of hierarchical macro-mesoporous silicon from easily accessible solid silica nanoparticles has been seldom reported. While we were writing up this paper, a short communication was published about the synthesis of macroporous silicon using magnesiothermic reduction process based on solid Stöber silica particles. However, the mesoporous structure feature of the macroporous silicon is not revealed and systematic investigation on the mechanism for the structure formation is not performed.[34]

Here in this work, three-dimensional (3D) hierarchical macro-/mesoporous silicon powders are synthesized through the magnesiothermic reduction process using zero-dimensional (0D) solid Stöber silica particles as the precursor. The reduction process is performed at 700 °C for 4 hours under Ar/H_2 atmosphere and the silica particles possess a uniform diameter of 410 nm. A facile self-templating process is governing the conversion from the zero-dimensional silica particles to the three-dimensional continuous silicon network during the magnesiothermic reduction. The macropores are formed by etching away the un-reacted silica particles after reduction. And the mesopores are generated within the three-dimensional silicon network during the reduction process. The introduction of both the macro and mesopores into the silicon powder significantly improves the cyclic and rate performance compared to the commercial nano-sized (30 nm in average) and μm-sized silicon (2 μm - 10 μm in average). Besides the application as lithium-ion battery anode, the use of the macro-/mesoporous silicon as photo catalytic hydrogen evolution catalyst is demonstrated as well.

RESULTS AND DISCUSSION

Figure 1a depicts the XRD patterns of the pristine SiO_2, the coarse product after magnesiothermic reduction, the "HCl-washing" silicon and "HF-etching" silicon. The weak broad diffraction peak located at approximately 23 ° shows that the obtained SiO_2 nanoparticles are amorphous. After magnesiothermic reduction, the coarse product shows six well-resolved diffraction peaks at 28.4 °, 47.3 °, 56.1 °, 69.1 °, 76.4 ° and 86.0 °, which can be well assigned to the (111), (220), (311), (400) , (331) and (422) planes of cubic phase of Si (JCPDS 27-1402). Besides, the peaks belonging to the MgO and Mg_2Si also appear. The results confirm that SiO_2 has been successfully converted to crystalline Si through magnesiothermic reduction. After washing with dilute HCl, the peaks of the Si are well preserved. However, all of the peaks of the MgO and Mg_2Si are not visible anymore, indicating successful removal of both MgO and Mg_2Si. Besides, the weak broad peak belonging to the amorphous silica is still observed, indicating the existence of un-reacted silica. With further etching by HF, the broad peak of the silica disappears and only the sharp peaks from the crystalline silicon are preserved. It indicates that the un-reacted silica has been totally removed by HF and only silicon is left. In the Raman spectrum of "HCl-washing" silicon and "HF-etching" silicon samples (Figure 1b), two peaks around 515 cm^{-1} and 940 cm^{-1} correspond to the characteristic peaks of elemental Si.[35, 36]
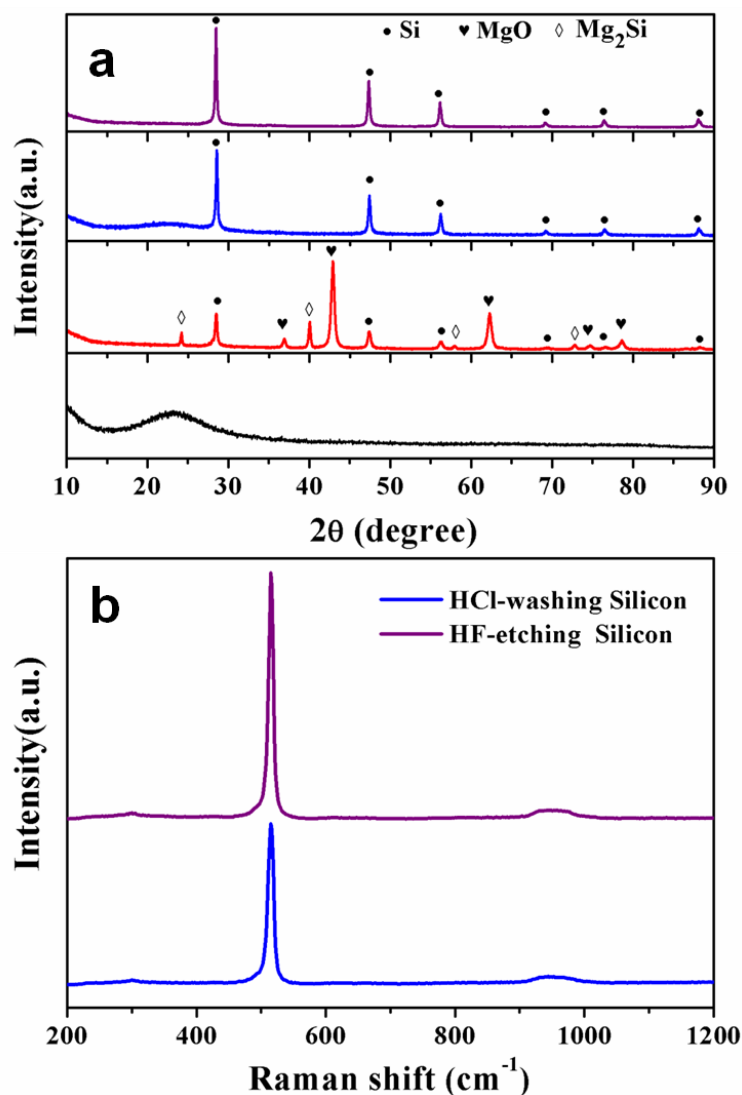
Figure 1. XRD patterns (a) and Raman spectra (b) of the obtained silicon products. Sample details: black (pristine SiO$_2$), red (coarse product after magnesiothermic reduction), blue ("HCl-washing" silicon), and purple ("HF-etching" silicon).

The morphologies of the pristine SiO$_2$, the "HCl-washing" silicon and the "HF-etching" silicon are exhibited in **Figure 2**. It can be seen that the as-prepared silica is composed of monodisperse solid sphere with the diameter of about 410 nm (Figure 2a, 2b). The "HCl-washing" silicon appears to preserve the same size and shape as the original SiO$_2$ spheres (Figure 2c). However, further high magnification SEM image (Figure 2d) shows that these spheres are actually interconnected with each other and the surface of the spheres become quite rough compared to the smooth surface of the pristine silica particles. The formation of

the interconnected structure is due to the exothermic process of the magnesiothermic reduction which causes fusion and agglomeration of the elemental silicon.[37,38] And the rough surface is a result of the etching process by liquid/gaseous magnesium at high temperature. Compared to the pristine silica and "HCl-washing" silicon, the "HF-etching" silicon exhibits a distinctly different structure. Three dimensional macroporous bulk structure with a pore size of about 380 nm in diameter is observed (Figure 2e, 2f). It can be seen that the HF treatment removes the spherical particles in the "HCl-washing" silicon sample, leaving the interconnected network behind. It suggests that the silica particles act as a self-template to guide the formation of the 3D macroporous continuous silicon network.
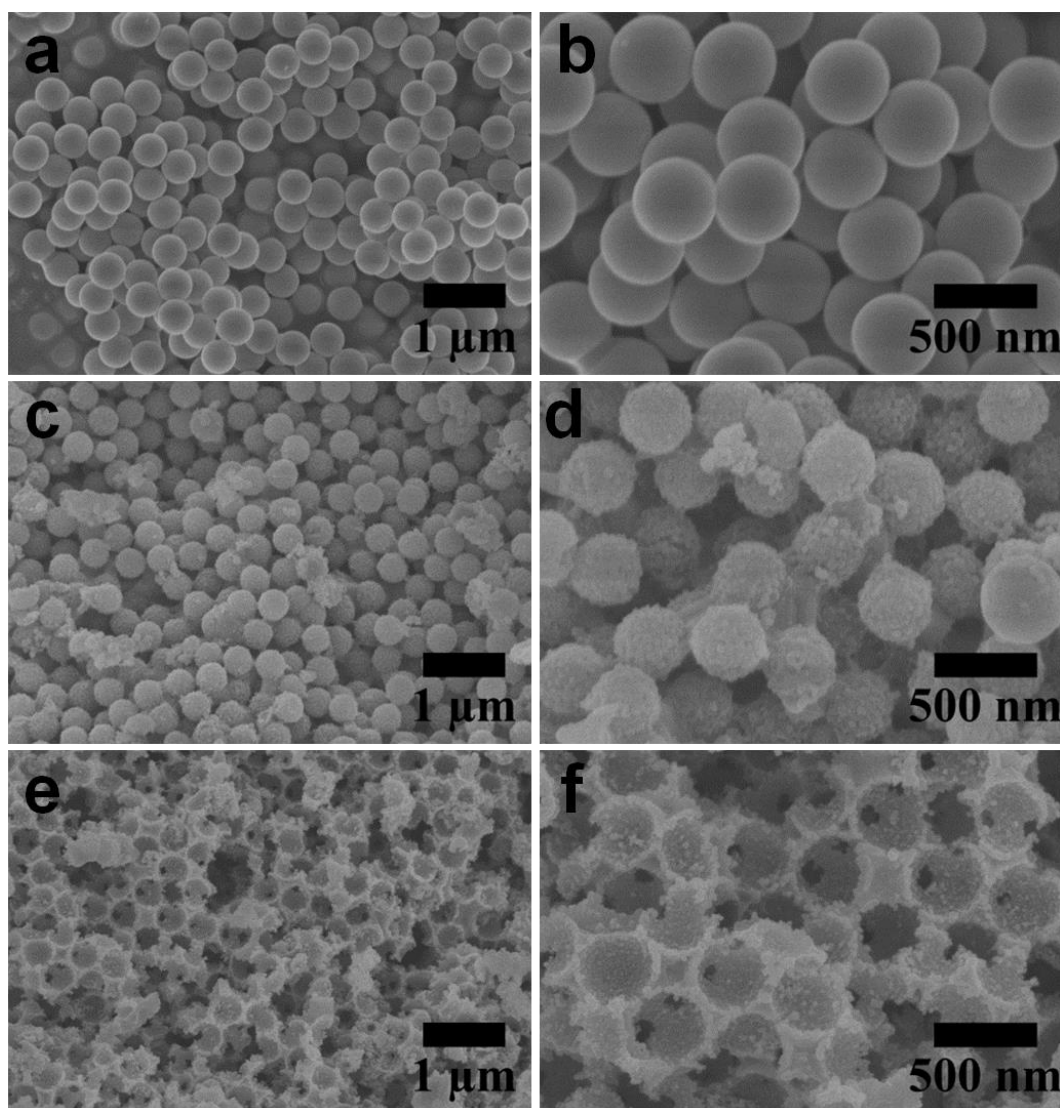

Figure 2. SEM images of the pristine SiO_2 (a, b), the "HCl-washing" silicon (c, d), and the "HF-etching"

silicon (e, f).

TEM is further applied to uncover the structure details of the three samples as shown in **Figure 3**. **Figure 3a** proves that the pristine SiO_2 is of smooth sphere with the diameter of 410 nm. It is consistent with the SEM images (Figure 2a, 2b). The HRTEM image and SAED pattern in Figure 3b indicate that the pristine SiO_2 spheres are amorphous, which agrees to the XRD results. Figure 3c unveils that the spheres in the "HCl-washing" silicon are interconnected with each other, which resemble the SEM image (Figure 2d). Furthermore, Figure 3c shows that some voids exist within the silica spheres. It is different from the solid structure of the pristine silica particles. The appearance of the voids originates from the etching process of the silica by the magnesium. It not only creates rough surface as shown by the SEM image (Figure 2d), but also generates voids inside the silica particles. The TEM image of the "HF-etching" silicon exhibits interconnected macroporous structure (Figure 3e), because the silica sphere within the "HCl-washing" silicon is removed by further HF etching. The HRTEM images combined with the SAED patterns of both the "HCl-washing" and "HF-etching" silicon indicate that the continuous network is composed of crystalline silicon (Figure 3d, 3f), which is proved by the XRD data as well. The d-spacing of 0.31 nm measured in the HRTEM images corresponds to the lattice fringe distance of the neighboring Si (111) crystal planes.[39]
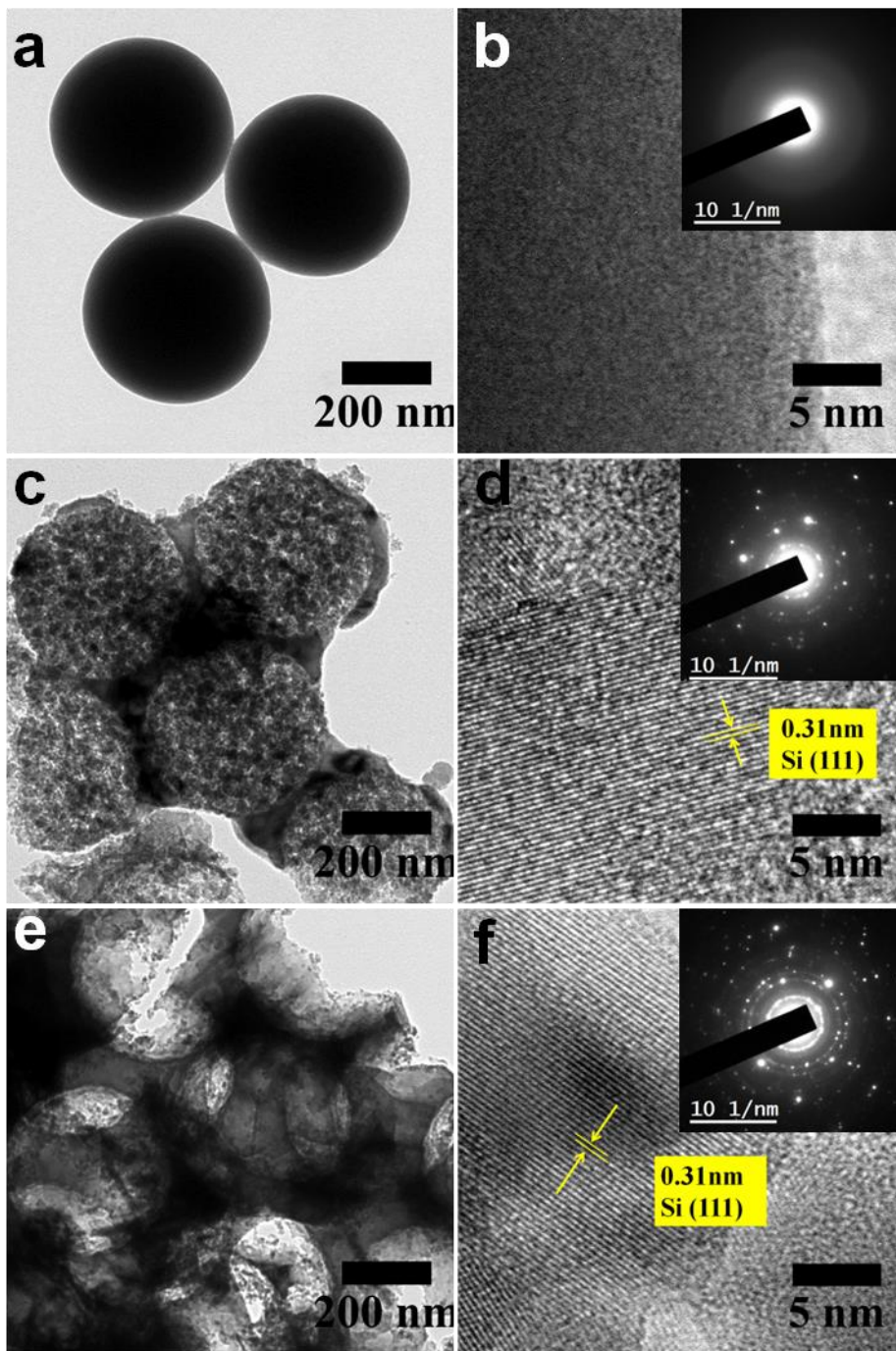
Figure 3. TEM images of the pristine SiO₂ (a), the "HCl-washing" silicon (b), and the "HF-etching" silicon (c); RTEM images and SAED patterns of the pristine SiO₂ (d), the "HCl-washing" silicon (e), and the "HF-etching" silicon (f).

The structure feature of the "HF-etching" silicon is also investigated by the Brunauer-Emmett-Teller (BET) measurement. As shown in **Figure 4a**, typical type III adsorption/desorption isotherm is obtained with a distinct hysteresis loop, indicating the presence of mesoporous microstructure.[40] The pore size

distribution profile in Figure 4b shows that average diameters of the major pores lie in the range between 20 nm and 50 nm. It further proves that the "HF-etching" silicon is of mesoporous. By combining the SEM and TEM images, it can be concluded that both macropores and mesopores exist in the "HF-etching" silicon. While the macropores refer to the voids created by the removal of the un-reacted silica particles; the mesopores reside within the 3D continuous silicon network. The mesopores make a major contribution to the relatively high specific surface area of the "HF-etching" silicon. It shows a specific surface area of 110.3 $m^2 g^{-1}$ and a pore volume of 0.57 $m^3 g^{-1}$, which are much higher than those of the commercial nano-sized silicon particles (40.2 $m^2 g^{-1}$ and 0.12 $m^3 g^{-1}$) as shown in **Figure S1**. Furthermore, the "HF-etching" silicon exhibits higher specific surface area than the "HCl-washing" silicon (79.2 $m^2 g^{-1}$ and 0.26 $m^3 g^{-1}$, **Figure S2**). But the pore size distribution patterns of the "HF-etching" silicon and "HCl-washing" silicon are quite similar. The results indicate that the HF etching process generates additional mesopores within the continuous network by removing the residual un-reacted silica.
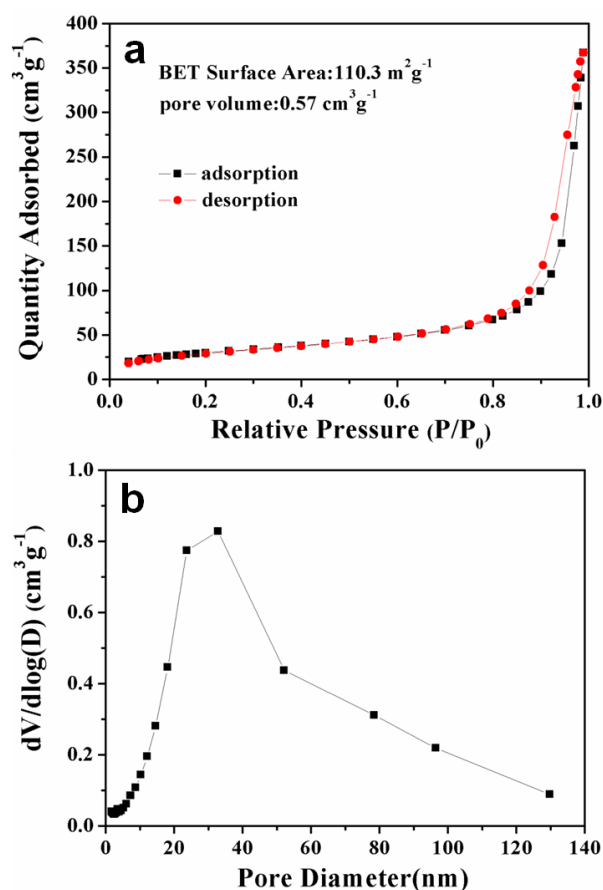
Figure 4. N_2 adsorption and desorption isotherms (a) and the corresponding BJH pore size distribution curve (b) of the "HF-etching" silicon.

Based on the systematic structure characterization addressed above, the mechanism for the formation of the 3D hierarchical macro-/mesoporous silicon is proposed as illustrated in **Figure 5**. The high temperature applied in the magnesiothermic reduction converts the solid magnesium powder into liquid magnesium melt. To minimize interfacial free energy, the silica particles form local colloidal crystal packing *via* a self-assembly process in the Mg melt. The Mg melt and vapor react with silica to form silicon, preferentially starting from the outer surface of the silica particles. The *in situ* generated silicon fuses together to build up a three-dimensional continuous network with a replica of the silica colloidal crystal. It is called a self-templating process because the silica particles exercise as a template to guide the morphology of the silicon, and source of the silicon simultaneously. The fusion process of the silicon leaves mesopores within the continuous network. Under the experimental condition addressed in this manuscript, the

11

conversion from silica to silicon is not complete probably due to limited temperature and time of the reduction process. As a result, un-reacted silica particles still reside in the holes of the 3D continuous silicon network. By removing the un-reacted silica with HF etching, the macropores are exposed to produce the 3D macro-/mesoporous silicon.
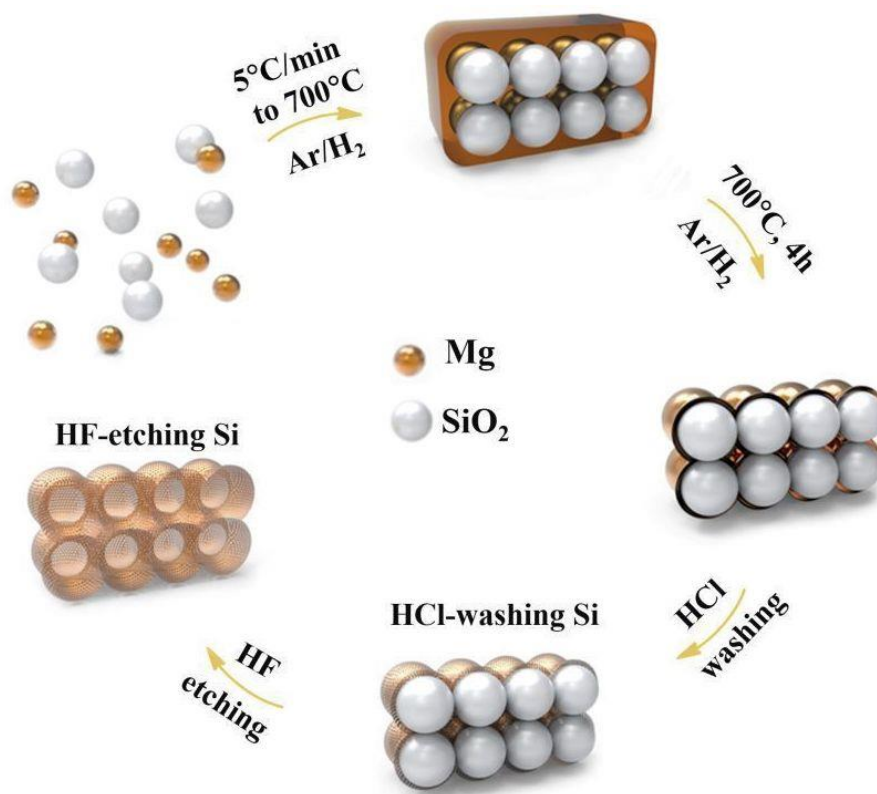

Figure 5. Schematic figure of the mechanism for the 3D hierarchical macro-/mesoporous silicon.

The applications of the 3D macroporous silicon as both LIB anode and photo catalytic hydrogen evolution catalyst are demonstrated. To better elucidate the role of the structure on the performance, commercial nano-sized silicon and μm-sized silicon are also tested as control samples to compare with the as-synthesized silicon. **Figure 6a** shows the representative first three consecutive cyclic voltammetry (CV) curves of the "HF-etching" silicon. In the lithiation scan, a broad irreversible reductive peak occurs at around 1.2 V in the first scan but disappears in subsequent cycles. It is attributed to the formation of the SEI film.[41, 42] In addition, there is a sharp reductive peak below 0.1 V in the first and subsequent scans, which corresponds to the transformation of silicon from a crystalline phase to an amorphous phase.[43, 44] In the

delithiation scan, two peaks are observed at around 0.34 V and 0.51 V in the first charge process and retained nearly the same positions in the following scans. The two peaks are ascribed to the delithiation of the Li-Si alloys.[45, 46] Meanwhile, increasing CV peak intensity is observed over the first few cycles due to an activation process of the silicon, which is also observed in previously reported silicon-based anode materials.[47-49] In general, the CV patterns of the "HF-etching" silicon are quite similar to the "HCl-washing" silicon, commercial nano-sized silicon and μm-sized silicon as shown in **Figure S3** (Figure S3a, S3c, and S3e). It indicates that the HF etching process does not modify the fundamental lithiation/delithiation processes significantly compared to the sample treated with only HCl-washing. Furthermore, it proves that the porous silicon obtained by the magnesiothermic reduction in this work exhibits almost identical electrochemical reaction mechanism as the typical commercial crystalline silicon particles.
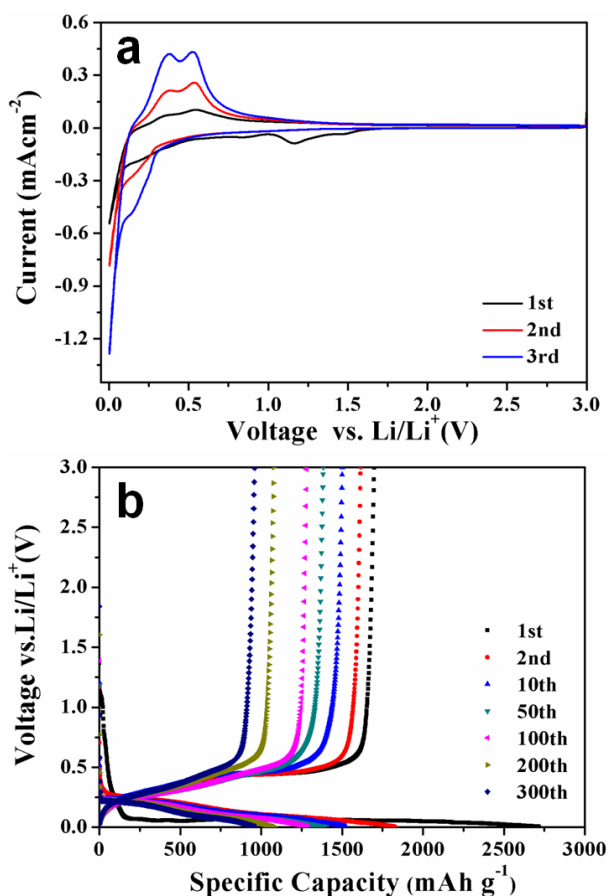

Figure 6. Cyclic voltammetry curves with a scanning rate of 0.2 mV sec^{-1} (a), and galvanostatic discharge-charge profiles (b) of the "HF-etching" silicon.

Figure 6b depicts representative discharge/charge profiles of the "HF-etching" silicon electrode for the 1st, 2nd, 10th, 50th, 100th, 200th and 300th cycle with a current density of 0.2 A g^{-1} between 0.005 V and 3.0 V. All the voltage plateaus in the discharge and charge curves agree well with the reductive and oxidative peaks in the CV curves (Figure 6a). During the first discharge process, a sloping voltage plateau between 1.2 V and 0.1 V indicates the formation of the stable SEI films, which disappears after subsequent cycles. It corresponds to the reductive peak around 1.2 V in the first cycle of the CV plots. The long and flat voltage plateaus below 0.1 V suggest the lithiation processes, which are consistent with the reductive peaks below 0.1 V in the CV plots.[50] In addition, the voltage plateaus located at about 0.5 V during the delithiation processes are also consistent with the oxidative peaks observed in the CV plots. The discharge/charge plateaus are well maintained after 300 cycles, indicating a very stable electrochemical process of the "HF-etching" silicon. The initial specific discharge and charge capacities of 2718 mA h g^{-1} and 1700 mA h g^{-1} are delivered, corresponding to an initial coulombic efficiency (CE) of 62.5 %. The moderate initial CE is probably related to the porous structure feature of the "HF-etching" silicon, where high specific surface area may facilitate the formation of the SEI films.[51, 52] As shown in Figure S3 (Figure S3b, S3d, and S3f), the representative discharge/charge curves of the "HCl-washing" silicon, commercial nano-sized and μm-sized silicon show very similar patterns to those of the "HF-etching" silicon. It is consistent with the CV results. But the capacities decay much faster than the "HF-etching" silicon, which implies an inferior cyclic performance.
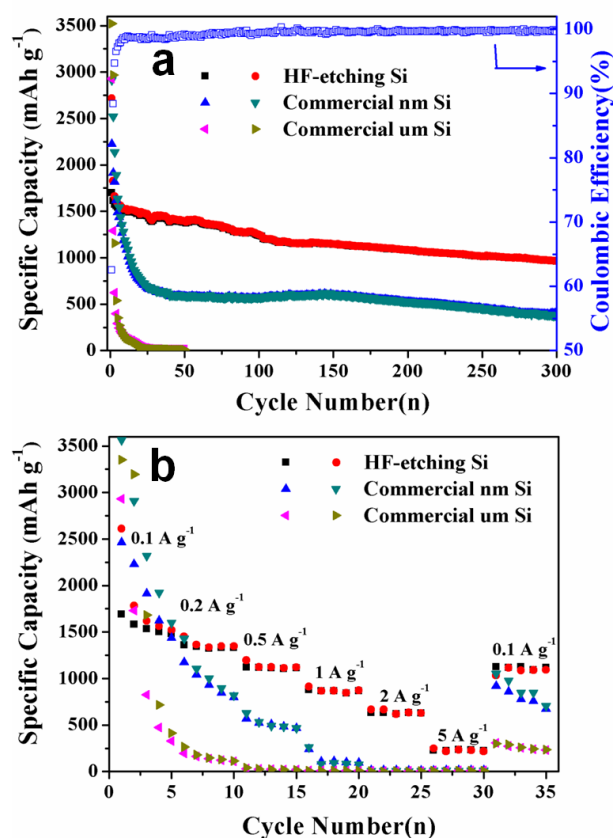
Figure 7. Cycling performance (a, current density: 0.2 A g^{-1}) and rate performance (b) of the "HF-etching"

silicon, commercial nano-sized Si and μm-sized Si.

The cyclic performance of the "HF-etching" silicon, "HCl-washing" silicon, commercial nano-sized Si

and μm-sized Si at a current density of 0.2 A g^{-1} are demonstrated in **Figure 7a, Figure S4** and summarized

in **Table 1**. It can be seen that the charge capacity of the "HF-etching" silicon is 1700 mAh g^{-1} at the first

cycle, which is retained at 1240 mAh g^{-1} after 100 cycles and 959 mAh g^{-1} after 300 cycles. It corresponds to

capacity retention values of 73 % and 56 %, respectively. Meanwhile, the coulombic efficiency of the

"HF-etching" silicon gradually increases from 62.5 % to 98.4 % at the 10th cycle and maintains the value

close to 100 % in the following cycles, reflecting a stable reversible electrochemical reaction. The stable

coulombic efficiency after 10 cycles is related to the porous structure which can effectively accommodate

the volume expansion. The originally formed SEI layer is less ruptured and the exposure of fresh silicon

surface to the electrolyte is inhibited. As a result, the formation of new SEI layer is avoided, which is one of

the major reasons for improved coulombic efficiency. Furthermore, it is also known that the SEI layer itself formed on the surface of the silicon makes important contributions to maintain reasonable cyclic stability and coulombic efficiency.[53, 54]

It should be emphasized that the mass loading density (1.4 mg cm^{-2}) of the "HF-etching" silicon electrode is much higher than many previously reported work.[55-58] This is one of the major reasons why the specific capacity reaches only around 1000 mAh g^{-1} after 300 cycles at 0.2 A g^{-1}. However, for the sake of the practical application of the silicon-based LIB anode, high mass loading is needed to realize decent energy output in full cell.[59] And a reasonable mass loading density of more than 1 mg cm^{-2} is required. Therefore, the work presented in this manuscript provides practically relevant cyclic performance of the Si anode. Compared to the "HF-etching" silicon, the commercial nano-sized and micro-sized silicon, and the "HCl-washing" silicon exhibit worse cyclic performance. The commercial nano-sized Si shows the initial discharge capacity of 2912 mAh g^{-1} and decreases to about 372 mAh g^{-1} after 300 cycles, corresponding to capacity retention of 18 %. And the commercial micro-sized Si shows even poor cyclic performance, where the capacity drops from 3524 mAh g^{-1} to 150 mAh g^{-1} after 10 cycles and even near zero just after 30 cycles. The "HCl-washing" silicon shows the initial discharge capacity of only 499 mAh g^{-1} and fades rapidly to about 20 mAh g^{-1} only after 30 cycles as shown in Figure S4. Besides, the cyclic ability of the "HF-etching" silicon is comparable or even better than some reported work on the porous silicon synthesized by similar magnesiothermic reduction process of the Stöber SiO$_2$.[30, 31]

Table 1. Summarized performance of the "HF-etching" Si, "HCl-washing" silicon, nano-sized Si, μm-sized Si and typical literature data

Samples	1st discharge/ charge capacity /mAh g^{-1}	Initial CE/%	Capacity retention/%	Current Density/A g^{-1}	Mass loading /mg cm^{-2}	Ref
HF-etching Si	2718/1700	62.5	73/56	0.2	1.4 (70 %)	this work
HCl-washing Si	499/189	37.8	6.9/-	0.2	1.4 (70 %)	this work
nano-sized Si	2912/2226	76.4	26/18	0.2	1.5 (70 %)	this work

μm-sized Si	3524/2930	83.1	0.3/-	0.2	1.8 (70 %)	this work
mesoporous Si	1844/1261	66.0	77/-	0.18	1.5 (50 %)	Ref 30
MPSSs	3105/-	-	70(50)	0.18	0.5–1.0 (70 %)	Ref 31

Note. The capacity retention refers to 100/300 cycles respectively, which is calculated against the initial charge capacity. The values in the brackets following the mass loading density number refer to the active material content within the electrode composition.

Considering that the "HF-etching" silicon is a bulk powder with the aggregate size of a few micrometers, it proves that the significantly improved cyclic stability compared to the commercial μm-sized silicon originates from the existence of the macro-/mesopores. It is worth noting that the μm-sized "HF-etching" silicon even shows cyclic performance superior to the nano-sized silicon powder. The result indicates that the incorporation of the macro-/mesopores exercise stronger effect than reducing Si particle size to improve the cyclic stability. Furthermore, the "HF-etching" silicon possesses much better cyclic stability than the "HCl-washing" silicon. It means that the formation of the macropores by etching away the un-reacted silica spheres is crucial for the cyclic performance. The macropores effectively accommodate the volume expansion and thus mitigate the mechanical stress induced by volume change. And the mesopores increase the electrolyte accessible surface area and shorten the lithium-ion diffusion length. Both macropores and mesopores lead to better electrode structure stability, enhanced electrochemical kinetics, and consequent improved cyclic performance.

Figure 7b and **Figure S5** depict the rate performance of different silicon materials. Generally, the "HF-etching" silicon shows the best cycling stability and rate performance among all samples, particularly at high current densities from 0.5 A g^{-1} to 5 A g^{-1}. In details, it delivers reversible capacities of about 1123 mAh g^{-1}, 879 mAh g^{-1}, 632 mAh g^{-1}, and 226 mAh g^{-1} at a discharge rate of 0.5 A g^{-1}, 1 A g^{-1}, 2 A g^{-1} and 5 A g^{-1} respectively. Nevertheless, the nano-sized Si electrode tested under the same conditions only displays 567 mAh g^{-1}, 241 mAh g^{-1}, 15 mAh g^{-1} and 9 mAh g^{-1} respectively. Furthermore, the micro-sized silicon exhibits much poorer rate performance, where the capacities drop to near zero from 0.5 A g^{-1}. Among the

different silicon samples, the "HCl-washing" silicon shows the worst rate performance where the capacities drop to near zero from 0.2 A g^{-1}, as shown in Figure S5. When the current density is reversed back to 0.1 A g^{-1} from 5 A g^{-1}, the capacity of the "HF-etching" silicon is almost fully recovered to the initial value (1123 mAh g^{-1}), indicating a good cyclic stability of the 3D macroporous silicon. The results suggest that the macro-/mesopores within the "HF-etching" silicon is beneficial for the electrolyte wetting and charge carrier transportation, leading to decreased charge polarization and improved rate capability. Additionally, the 3D continuous silicon network also reduces the charge carrier transportation resistance due to limited grain boundary effect.

The capacity of the macro-/mesoporous silicon originated from the formation of the electrochemical double layer capacitor is measured and analyzed.[60, 61] The double layer capacitor results exhibited in **Figure S7** indicate that the capacities contributed by the double layer capacitor process are very limited.[62] It is also consistent with previous studies on the carbon based double layer capacitors, which implies that the porous silicon synthesized in this work possesses rather limited capacities from the double layer capacitance process. [63, 64]
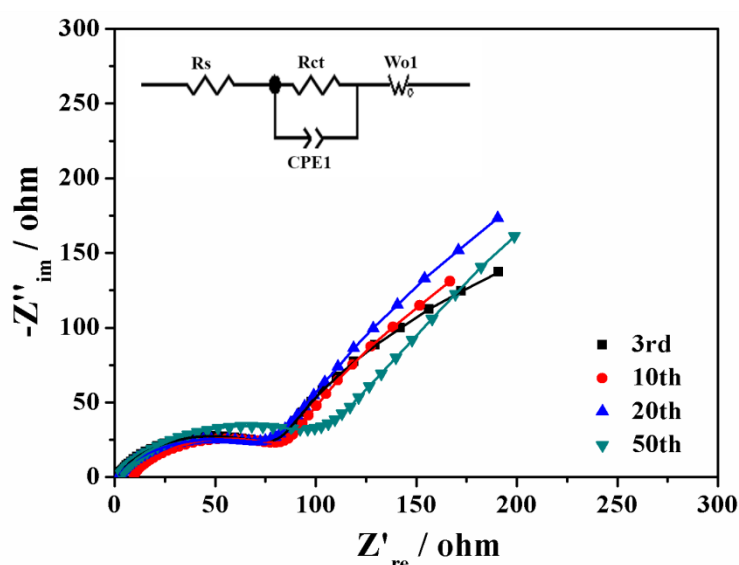

Figure 8. Nyquist plots of the "HF-etching" silicon anode after the 3, 10, 20 and 50 discharge/charge

cycles at the current density of 0.2 A g^{-1}.

EIS measurements are carried out to analyze the resistance change of the "HF-etching" silicon electrode with increasing cycles. The Nyquist plots at the fully de-lithiated state (charged to 3.0 V) after 3, 10, 20 and 50 cycles are shown in **Figure 8**. The high-frequency semicircle in the EIS profiles stands for charge transfer resistance while the low-frequency line is corresponding to the Warburg impedance owing to the ion diffusion-controlled process.[39, 65-67] The equivalent circuit model (inset in Figure 8) represents the electrochemical process of the "HF-etching" silicon anode roughly by a single Rct (charge transfer resistance) with CPE$_l$ and Warburg element (W$_o$) for the diffusion of lithium ions. The Rct of the electrode after 3, 10, 20 and 50 cycles is 69.4 Ω, 70.6 Ω, 69.9 Ω and 93.1 Ω respectively. The small change of Rct during the first 50 cycles implies an excellent structural stability of the "HF-etching" silicon materials as well as a good electronic contact between the active materials and the current collector. The EIS results are in good agreement with the cycling performance (Figure 7a).
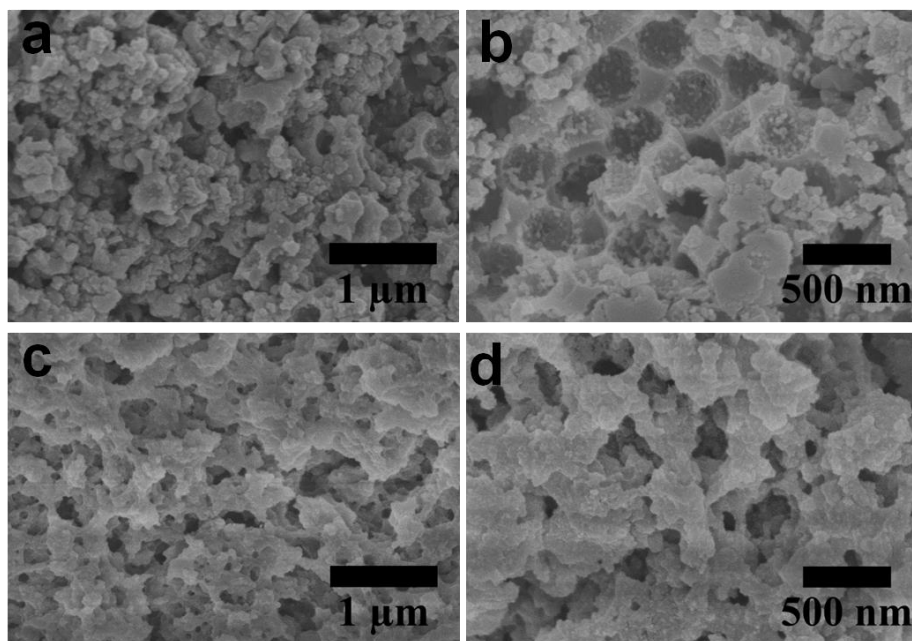

Figure 9. SEM images of the "HF-etching" silicon electrode before (a, b) and after 300 cycles (c, d).

The morphology change of the "HF-etching" silicon electrode after 300 cycles is characterized by SEM (**Figure 9**). As shown in Figure 9a and 9b, the pristine "HF-etching" silicon electrode shows

continuous porous structure. After 300 cycles, the electrode still maintains the original porous structure (Figure 9c and 9d). Furthermore, it is found that major part of the nano-sized silicon electrode is peeled off from the copper current collector after 300 cycles. While the "HF-etching" silicon electrode still remains intact under the same condition. Both the SEM and optical imaging results confirm that the "HF-etching" silicon possesses extraordinary structure stability. The hierarchical macro-/mesoporous structures effectively accommodate the volume change and release the mechanical stress, leading to significantly improved cyclic performance.

Besides the application as LIB anode, photocatalytic hydrogen evolution performance of the "HF-etching" silicon is also investigated because Si has a relative narrow band gap and can absorb more visible light.[68-71] The UV-Vis spectra (**Figure S6**) indicate that the "HF-etching" silicon exhibits stronger absorption in wider wavelength range than the nano-sized and μm-sized Si, which is related to its porous structure. As shown in **Figure 10**, The "HF-etching" silicon exhibits the best photocatalytic performance under all of the three testing conditions, compared to the commercial nano-sized and μm-sized Si. The enhanced catalytic performance of the "HF-etching" silicon originates from the hierarchical macro-/mesoporous structure feature and associated high specific surface area. Specifically, around 280 μmol/g hydrogen is generated after 5 hours illumination under full spectrum light illumination, which is more than 40 % higher than those of the nano-sized and micro-sized silicon. Regarding the speed of the hydrogen evolution, the "HF-etching" silicon is around 40 % faster than the nano-sized and micro-sized silicon under the UV-Vis illumination condition. The results indicate that this 3D macro-/mesoporous silicon demonstrates a great potential as photo catalytic hydrogen evolution catalyst.
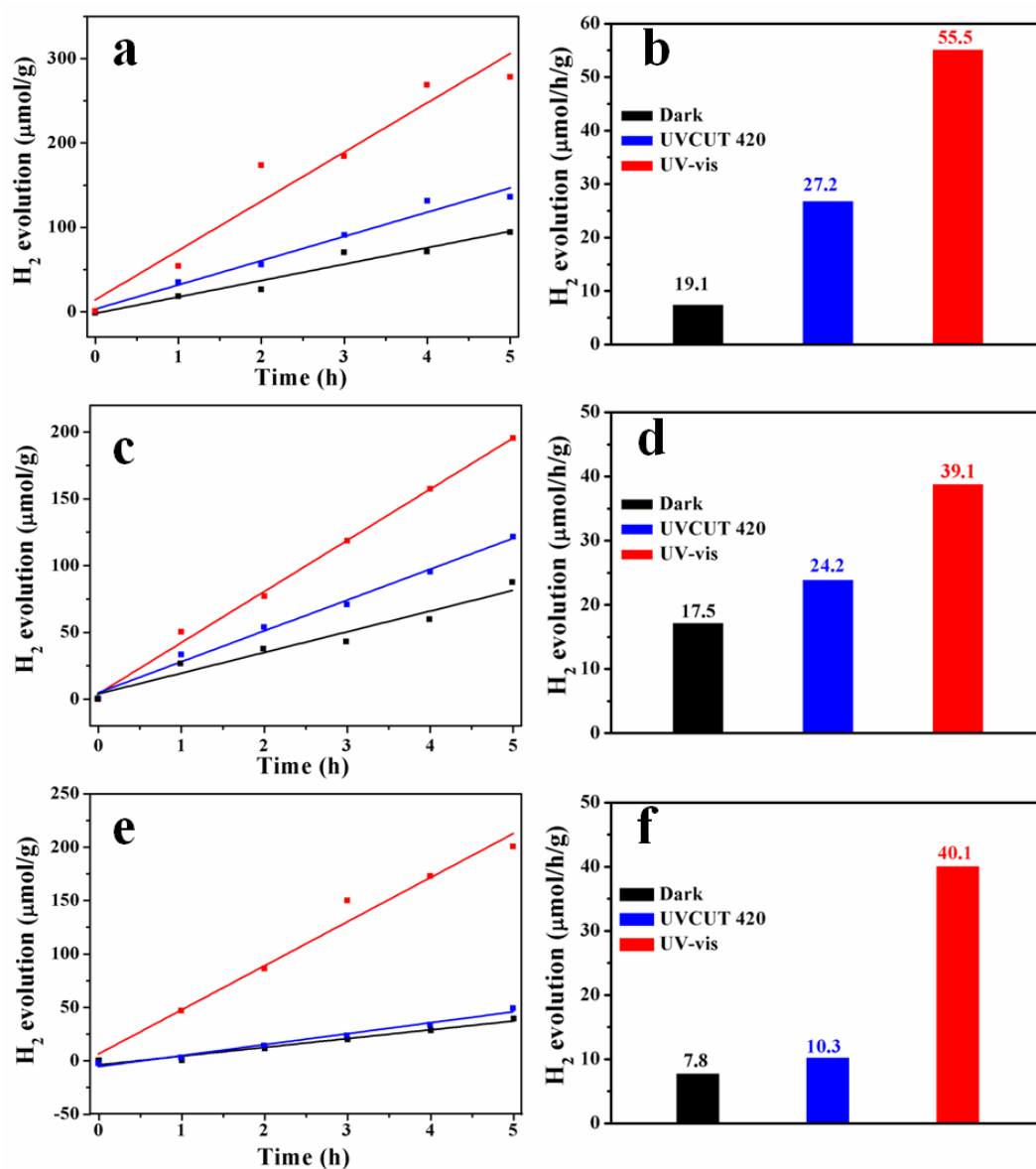
Figure 10. Photocatalytic hydrogen evolution performance of the "HF-etching" silicon (a, b), commercial nano-sized Si (c, d), and commercial μm-sized Si (e and f) under UV (red), visible light illumination (blue) and in darkness (black).

CONCLUSIONS

In summary, 3D hierarchical macro-/mesoporous silicon has been successfully synthesized *via* a magnesiothermic reduction process using 0D Stöber silica particles as the starting material. Based on the systematic structure characterization of the "HCl-washing" silicon and "HF-etching" silicon, a self-templating mechanism responsible for the hierarchical porous silicon is proposed. Well crystallized

porous silicon is obtained after the magnesiothermic reduction as confirmed by XRD, HRTEM, and SAED characterization. Both SEM and TEM images indicate the presence of the three-dimensional macroporous Si network, where the macropores is formed due to the removal of the un-reacted silica particles by HF etching. The nitrogen adsorption/desorption measurement reveals that mesopores coexist with the macropores, which are supposed to be within the continuous Si network. Increased specific surface area is measured due to the presence of the mesopores. Compared to the commercial nano-sized and μm-sized silicon particles, the macro-/mesoporous silicon exhibits significantly improved cyclic and rate performance. A reversible capacity of 959 mAh g^{-1} is retained after 300 cycles at 0.2 A g^{-1} with a high mass loading density of 1.4 mg cm^{-2}. At the high current density of 2 A g^{-1}, a reversible capacity of 632 mAh g^{-1} is still achieved. The macropores accommodate the drastic volume change of the Si upon lithiation to effectively mitigate the mechanical stress. And the mesopores enhance the electrochemical kinetics due to their large specific surface area. Better electrode structure stability is confirmed by the SEM images before and after 300 cycles, which is responsible for the good cyclic performance. The photocatalytic hydrogen evolution test shows that the macro-/mesoporous silicon possesses much better performance than the nano-sized and μm-sized silicon particles under different illumination conditions due to its large specific surface area. The work presented in this manuscript will boost the development of the practically relevant Si based anode for future high performance lithium-ion batteries. It will be also inspiring for other Si based functional materials fields. Further systematic studies on the fundamental understanding and application of the macro-/porous silicon based on the magnesiothermic reduction are in progress and will be addressed in future publications.

METHODS

Materials. All chemicals were used as received without further purification. Tetraethyl orthosilicate (TEOS, $\geq$ 96 %), ethanol (EtOH, $\geq$ 99.5 %) , ammonium hydroxide (NH$_3$ H$_2$O, 25 % - 28 %) , Magnesium (Mg, 100 mesh - 200 mesh, $\geq$ 99 %), hydrochloric acid (HCl, 36.0 % - 38.0 %) and hydrofluoric acid (HF, $\geq$

40 %) were purchased from Sinopharm Group Co., Ltd. Sodium alginate was obtained from Aladdin. Conductive carbon black (Super P, ≥ 99 %) was bought from Alfa Aesar. Nano-sized silicon (30 nm, > 99.9 %) was purchased from HaoTian Nano Technology (Shanghai) Co., Ltd. Micro-sized silicon (2 μm - 10 μm, > 99.9 %) was donated by Fuzhou Sunout Energy & Material Technology Inc.

Sample Preparation. The nano-sized silica (SiO_2) spheres were synthesized by a modified Stöber process.[72] Firstly, 9 mL $NH_3 \cdot H_2O$, 16.25 mL ethanol, and 24.75 mL de-ionized water were mixed at room temperature with a stirring speed of 1100 rpm to form a clear solution, named as solution A. Next, solution B was prepared by adding 4.5 mL TEOS to 45.5 mL ethanol. Solution B was thereafter added within 1 minute into the solution A with a stirring speed of 400 rpm. The final mixture was kept stirring for 2 hours. After reaction, the final products were collected after centrifugation and washed with absolute ethanol for four times, followed by drying in vacuum oven at 80 °C for 4 hours.

The white as-prepared SiO_2 powder was firstly thoroughly ground in an agate mortar and then mixed together with Mg powder with a 1:1 mass ratio to get a homogeneous powder mixture with gray color. The powder mixture was put in a crucible boat and heated under Ar/H_2 flow (volume ratio: 95/5, 0.3 mL/min) in a tube furnace. The temperature profile was programmed with a temperature rise from room temperature to 700 °C at a ramp rate of 5 °C/min and maintained for 4 hours, followed by cooling to room temperature at 5 °C/min. After magnesiothermic reduction, the obtained brown yellow powder was put in 1 M HCl aqueous solution overnight to remove MgO and Mg_2Si. Thereafter, the powder was collected by centrifugation, washed with de-ionized water, and vacuum dried at 80 °C overnight, which was indexed as "HCl-washing" silicon. Alternatively, the powder washed with HCl was further treated with 4 % HF for 1 hour to remove unreacted SiO_2. After etching with HF, the powder was rinsed with de-ionized water for several times and further dried in vacuum oven for 8 hours at 80 °C. The sample etched with HF was named as "HF-etching" silicon corresponding to the "HCl-washing" silicon.

Physical Characterization. The crystallographic phase of the samples was characterized by Bruker AXS D8 Advance X-ray powder diffractometer ($\lambda = 1.5406$ Å, 2.2 kW) with a 2θ ranging from 10 ° to 90 ° using Cu $K_{\alpha 1}$ radiation and a scan rate of 3 ° min^{-1}. The morphology of the porous Si was investigated with field emission scanning electron microscopy (Hitachi S4800) at an accelerating voltage of 4 kV. Transmission electron microscopy (TEM) images were collected using JEOL JEM-2100F TEM operated at 200 kV. The specific surface area measurement was carried out based on N_2 adsorption desorption test with Micromeritics ASAP2020 Accelerated Surface Area and Porosimetry System. The Raman spectra were obtained using Renishaw inVia-reflex spectrometer. The UV-Vis Measurements were carried out using Lambda 950. $BaSO_4$ was exploited as a substrate, which was prepared by pressing certain amount of $BaSO_4$ into pellets at the bottom of sample vial. Thereafter, around 50 mg of the sample powder was pressed into a pellet and put on the surface of the $BaSO_4$ pellet substrate.

Electrochemical Tests. The LIB electrodes were prepared by casting the aqueous slurry on copper foil containing 70 % active material (HCl-washing silicon, HF-etching silicon, nano-sized silicon, or μm-sized silicon), 20 % sodium alginate binder and 10 % Super P by mass. The typical mass loading density regarding the silicon content was controlled to be around 1.4 mg cm^{-2}. After casting, the slurry was dried in oven at 40 °C for 8 hours. Thereafter, the electrode sheet was pressed and punched into spherical electrode with a diameter of 13 mm. The mass loading of the individual electrode was weighed using a balance with the resolution of 0.01 mg. After weighing, the electrodes were further dried at 80 °C for 4 hours before coin cell assembly. CR 2032 type coin cell was assembled in argon filled glove box (< 0.1 ppm H_2O and < 0.1 ppm O_2) using lithium foil as a counter electrode. Commercial electrolyte from Zhangjiagang Guotai-Huarong Chemical New Material Co., Ltd. was used; where 1.0 M $LiPF_6$ was dissolved in a mixture of ethylene carbonate (EC) and diethyl carbonate (DMC) (1:1 v/v) with 5 wt% fluoroethylene carbonate (FEC). Cycling performance and rate performance measurements were conducted with a fixed voltage

window between 0.005 V and 3.0 V (vs. Li/Li$^+$) on a multichannel Land Battery Test System. The cycle performance test was carried out at a current density of 0.2 C (1 C = 1 A g^{-1}). The rate performance was measured at the current density sequence of 0.1C, 0.2 C, 0.5 C, 1.0 C, 2.0 C, 5.0 C and 0.1 C. The specific capacity was calculated based on the mass of the active material only. The cyclic voltammetry (CV) scans and electrochemical impedance spectroscopy (EIS) data were collected on a Solartron Analytical. For CV, a voltage of 0.001 V- 3.0 V and a scan rate of 0.2 mV sec^{-1} were used, and EIS was performed between 0.001 Hz and 1 MHz with amplitude of 10 mV.

The electrochemical double layer behavior of the macro-/mesoporous Si powder was evaluated based on systematic supercapacitor. Working electrodes were fabricated by casting aqueous slurry of the porous silicon powder on nickel foam, which had the same composition as the slurry for the LIB anode. The mass of the active material loaded for each plate was in the range between 2 mg and 3 mg. CR2032 type coin cell was assembled with the same protocol as the LIB anode. Cycling performance measurement was conducted for 6 cycles with voltage window between 0.005 V and 2.7 V at a current density of 0.1 C (100 mA g^{-1}) on a multichannel Land Battery Test System.

Photocatalytic Hydrogen Evolution Performance Test. Photo catalytic activity measurement was carried out according to the following procedure. 50 mg of sample powders of the "HF-etching" silicon, commercial nano-sized silicon and μm-sized silicon were dispersed into 120 ml aqueous methanol solution with the volume concentration of 25 vol % in a closed gas circulation system (Perfect Light Company Labsolar-III (AG)). The UV-visible light irradiations were received from a 300 W Xe lamp (Perfect Light Company Solaredge 700) without and with a UVCUT-420 nm filter (CE Aulight. Inc). The evolved gases were detected *in situ* by using an online gas chromatograph (GC-2014C, Shimadzu) equipped with a thermal conductivity detector (TCD).

ASSOCIATED CONTENT

SUPPORTING INFORMATION

The supporting information is available free of charge *via* the Internet at http://pubs.acs.org. Porosity of commercial nano-sized silicon, porosity of the "HCl-washing" silicon, Cyclic voltammetry and galvanostatic discharge/charge profiles of the "HCl-washing" silicon, commercial nano-sized silicon and micrometer-sized silicon, cycling and rate performance of the "HCl-washing" silicon, UV-Vis spectra of the "HF-etching" silicon, commercial nano-sized silicon and micrometer-sized silicon, and cycling performance of the "HF-etching" silicon as systematic double layer capacitance.

AUTHOR INFORMATION

Corresponding author

*E-mail address: chengyj@nimte.ac.cn

ORCID

Ya-Jun Cheng: 0000-0002-0932-295X

NOTES

The authors declare no competing financial interest.

REFERENCES

1. Bisi, O.; Ossicini, S.; Pavesi, L. Porous Silicon: A Quantum Sponge Structure for Silicon Based Optoelectronics. *Surf. Sci. Rep.* **2000,** *38*, 1-126.
2. Anglin, E. J.; Cheng, L.; Freeman, W. R.; Sailor, M. J. Porous Silicon in Drug Delivery Devices and Materials. *Adv. Drug Delivery Rev.* **2008,** *60*, 1266-1277.

3.   Huger, E.; Dorrer, L.; Rahn, J.; Panzner, T.; Stahn, J.; Lilienkamp, G.; Schmidt, H. Lithium Transport through Nanosized Amorphous Silicon Layers. *Nano Lett.* **2013,** *13*, 1237-1244.

4.   Harraz, F. A. Porous Silicon Chemical Sensors and Biosensors: A Review. *Sens. Actuators, B* **2014,** *202*, 897-912.

5.   Zuo, X.; Zhu, J.; Müller-Buschbaum, P.; Cheng, Y.-J. Silicon Based Lithium-Ion Battery Anodes: A Chronicle Perspective Review. *Nano Energy* **2017,** *31*, 113-143.

6.   Wang, B.; Li, X. L.; Zhang, X. F.; Luo, B.; Jin, M. H.; Liang, M. H.; Dayeh, S. A.; Picraux, S. T.; Zhi, L. J. Adaptable Silicon-Carbon Nanocables Sandwiched between Reduced Graphene Oxide Sheets as Lithium Ion Battery Anodes. *ACS Nano* **2013,** *7*, 1437-1445.

7.   Liang, B.; Liu, Y.; Xu, Y. Silicon-Based Materials as High Capacity Anodes for Next Generation Lithium Ion Batteries. *J. Power Sources* **2014,** *267*, 469-490.

8.   Rahman, M. A.; Song, G.; Bhatt, A. I.; Wong, Y. C.; Wen, C. Nanostructured Silicon Anodes for High-Performance Lithium-Ion Batteries. *Adv. Funct. Mater.* **2016,** *26*, 647-678.

9.   Zhao, L.; Dvorak, D. J.; Obrovac, M. N. Layered Amorphous Silicon as Negative Electrodes in Lithium-Ion Batteries. *J. Power Sources* **2016,** *332*, 290-298.

10. Hu, Z.; Zhang, S.; Zhang, C.; Cui, G. High Performance Germanium-Based Anode Materials. *Coord. Chem. Rev.* **2016,** *326*, 34-85.

11. Cui, G.; Gu, L.; Zhi, L.; Kaskhedikar, N.; van Aken, P. A.; Müllen, K.; Maier, J. A Germanium-Carbon Nanocomposite Material for Lithium Batteries. *Adv. Mater.* **2008,** *20*, 3079-3083.

12. Cho, J. Porous Si Anode Materials for Lithium Rechargeable Batteries. *J. Mater. Chem.* **2010,** *20*, 4009-4014.

13. Li, X.; Gu, M.; Hu, S.; Kennard, R.; Yan, P.; Chen, X.; Wang, C.; Sailor, M. J.; Zhang, J.-G.; Liu, J. Mesoporous Silicon Sponge as an Anti-Pulverization Structure for High-Performance Lithium-Ion Battery Anodes. *Nat. Commun.* **2014,** *5*, 4105.

14. Ashuri, M.; He, Q.; Shaw, L. L. Silicon as a Potential Anode Material for Li-Ion Batteries: Where Size, Geometry and Structure Matter. *Nanoscale* **2016,** *8*, 74-103.

15. Unagami, T. Formation Mechanism of Porous Silicon Layer by Anodization in Hf Solution. *J. Electrochem. Soc.* **1980,** *127*, 476-483.

16. Zhao, Y.; Liu, X.; Li, H.; Zhai, T.; Zhou, H. Hierarchical Micro/Nano Porous Silicon Li-Ion Battery Anodes. *Chem. Commun.* **2012,** *48*, 5079-5081.

17. Díaz-Torres, E.; Romero-Paredes, G.; Peña-Sierra, R.; Ávila-García, A. Formation and Characterization of Porous Silicon Films Obtained by Catalyzed Vapor-Chemical Etching. *Mater. Sci. Semicond. Process.* **2015,** *40*, 533-538.

18. Azeredo, B. P.; Lin, Y.-W.; Avagyan, A.; Sivaguru, M.; Hsu, K.; Ferreira, P. Direct Imprinting of Porous Silicon *via* Metal-Assisted Chemical Etching. *Adv. Funct. Mater.* **2016,** *26*, 2929-2939.

19. Jiang, Z.; Li, C.; Hao, S.; Zhu, K.; Zhang, P. An Easy Way for Preparing High Performance Porous Silicon Powder by Acid Etching Al–Si Alloy Powder for Lithium Ion Battery. *Electrochim. Acta* **2014,** *115*, 393-398.

20. Feng, J.; Zhang, Z.; Ci, L.; Zhai, W.; Ai, Q.; Xiong, S. Chemical Dealloying Synthesis of Porous Silicon Anchored by *in situ* Generated Graphene Sheets as Anode Material for Lithium-Ion Batteries. *J. Power Sources* **2015,** *287*, 177-183.

21. He, W.; Tian, H.; Xin, F.; Han, W. Scalable Fabrication of Micro-Sized Bulk Porous Si from Fe-Si Alloy as a High Performance Anode for Lithium-Ion Batteries. *J. Mater. Chem. A* **2015,** *3*, 17956-17962.

22. Wang, X.; Wu, Y.; Liu, X.; Chen, J.; Zhen, C.; Ma, L.; Hou, D. A Template-Based Method for Preparing Ordered Porous Silicon. *J. Porous Mater.* **2015,** *22*, 1431-1435.

23. Kim, H.; Han, B.; Choo, J.; Cho, J. Three-Dimensional Porous Silicon Particles for Use in High-Performance Lithium Secondary Batteries. *Angew. Chem. Int. Ed. Engl.* **2008,** *47*, 10151-4.

24. Jeong, J.-H.; Kim, K.-H.; Jung, D.-W.; Kim, K.; Lee, S.-M.; Oh, E.-S. High-Performance Characteristics of Silicon Inverse Opal Synthesized by the Simple Magnesium Reduction as Anodes for Lithium-Ion Batteries. *J. Power Sources* **2015,** *300*, 182-189.

25. Bao, Z.; Weatherspoon, M. R.; Shian, S.; Cai, Y.; Graham, P. D.; Allan, S. M.; Ahmad, G.; Dickerson, M. B.; Church,

B. C.; Kang, Z.; Abernathy Iii, H. W.; Summers, C. J.; Liu, M.; Sandhage, K. H. Chemical Reduction of Three-Dimensional Silica Micro-Assemblies into Microporous Silicon Replicas. *Nature* **2007,** *446*, 172-175.

26. Jia, H.; Gao, P.; Yang, J.; Wang, J.; Nuli, Y.; Yang, Z. Novel Three-Dimensional Mesoporous Silicon for High Power Lithium-Ion Battery Anode Material. *Adv. Energy Mater.* **2011,** *1*, 1036-1039.

27. Hong, I.; Scrosati, B.; Croce, F. Mesoporous, Si/C Composite Anode for Li Battery Obtained by 'Magnesium-Thermal' Reduction Process. *Solid State Ionics* **2013,** *232*, 24-28.

28. Kim, K. H.; Lee, D. J.; Cho, K. M.; Kim, S. J.; Park, J.-K.; Jung, H.-T. Complete Magnesiothermic Reduction Reaction of Vertically Aligned Mesoporous Silica Channels to Form Pure Silicon Nanoparticles. *Sci. Rep.* **2015,** *5*, 9014.

29. Yu, Y.; Gu, L.; Zhu, C.; Tsukimoto, S.; van Aken, P. A.; Maier, J. Reversible Storage of Lithium in Silver-Coated Three-Dimensional Macroporous Silicon. *Adv. Mater.* **2010,** *22*, 2247-50.

30. Zhong, H.; Zhan, H.; Zhou, Y.-H. Synthesis of Nanosized Mesoporous Silicon by Magnesium-Thermal Method Used as Anode Material for Lithium Ion Battery. *J. Power Sources* **2014,** *262*, 10-14.

31. Wang, W.; Favors, Z.; Ionescu, R.; Ye, R.; Bay, H. H.; Ozkan, M.; Ozkan, C. S. Monodisperse Porous Silicon Spheres as Anode Materials for Lithium Ion Batteries. *Sci. Rep.* **2015,** *5*, 6.

32. Li, X.; Yan, P.; Arey, B. W.; Luo, W.; Ji, X.; Wang, C.; Liu, J.; Zhang, J.-G. A Stable Nanoporous Silicon Anode Prepared by Modified Magnesiothermic Reactions. *Nano Energy* **2016,** *20*, 68-75.

33. Xiao, Q.; Gu, M.; Yang, H.; Li, B.; Zhang, C.; Liu, Y.; Liu, F.; Dai, F.; Yang, L.; Liu, Z.; Xiao, X.; Liu, G.; Zhao, P.; Zhang, S.; Wang, C.; Lu, Y.; Cai, M. Inward Lithium-Ion Breathing of Hierarchically Porous Silicon Anodes. *Nat. Commun.* **2015,** *6*, 8844.

34. Wu, H.; Du, N.; Shi, X.; Yang, D. Rational Design of Three-Dimensional Macroporous Silicon as High Performance Li-Ion Battery Anodes with Long Cycle Life. *J. Power Sources* **2016,** *331*, 76-81.

35. Li, B.; Yang, S.; Li, S.; Wang, B.; Liu, J. From Commercial Sponge toward 3d Graphene–Silicon Networks for Superior Lithium Storage. *Adv. Energy Mater.* **2015,** *5*, 1500289.

36. Xu, Q.; Li, J.-Y.; Sun, J.-K.; Yin, Y.-X.; Wan, L.-J.; Guo, Y.-G. Watermelon-Inspired Si/C Microspheres with Hierarchical Buffer Structures for Densely Compacted Lithium-Ion Battery Anodes. *Adv. Energy Mater.* **2016**, 1601481.

37. Shi, L.; Wang, W.; Wang, A.; Yuan, K.; Yang, Y. Understanding the Impact Mechanism of the Thermal Effect on the Porous Silicon Anode Material Preparation *via* Magnesiothermic Reduction. *J. Alloys Compd.* **2016,** *661*, 27-37.

38. Liu, N.; Huo, K.; McDowell, M. T.; Zhao, J.; Cui, Y. Rice Husks as a Sustainable Source of Nanostructured Silicon for High Performance Li-Ion Battery Anodes. *Sci. Rep.* **2013,** *3*, 1919.

39. Zhang, Y.-C.; You, Y.; Xin, S.; Yin, Y.-X.; Zhang, J.; Wang, P.; Zheng, X.-s.; Cao, F.-F.; Guo, Y.-G. Rice Husk-Derived Hierarchical Silicon/Nitrogen-Doped Carbon/Carbon Nanotube Spheres as Low-Cost and High-Capacity Anodes for Lithium-Ion Batteries. *Nano Energy* **2016,** *25*, 120-127.

40. Yi, Z.; Han, Q.; Zan, P.; Cheng, Y.; Wu, Y.; Wang, L. Facile Fabrication of Sno2@Tio2core–Shell Structures as Anode Materials for Lithium-Ion Batteries. *J. Mater. Chem. A* **2016,** *4*, 12850-12857.

41. Zhou, X.; Yin, Y.-X.; Wan, L.-J.; Guo, Y.-G. Facile Synthesis of Silicon Nanoparticles Inserted into Graphene Sheets as Improved Anode Materials for Lithium-Ion Batteries. *Chem. Commun.* **2012,** *48*, 2198-2200.

42. Wang, L.; Gao, B.; Peng, C.; Peng, X.; Fu, J.; Chu, P. K.; Huo, K. Bamboo Leaf Derived Ultrafine Si Nanoparticles and Si/C Nanocomposites for High-Performance Li-Ion Battery Anodes. *Nanoscale* **2015,** *7*, 13840-13847.

43. Favors, Z.; Wang, W.; Bay, H. H.; Mutlu, Z.; Ahmed, K.; Liu, C.; Ozkan, M.; Ozkan, C. S. Scalable Synthesis of Nano-Silicon from Beach Sand for Long Cycle Life Li-Ion Batteries. *Sci Rep* **2014,** *4*, 5623.

44. Wang, B.; Li, X. L.; Luo, B.; Jia, Y. Y.; Zhi, L. J. One-Dimensional/Two-Dimensional Hybridization for Self-Supported Binder-Free Silicon-Based Lithium Ion Battery Anodes. *Nanoscale* **2013,** *5*, 1470-1474.

45. Sun, L.; Su, T.; Xu, L.; Du, H.-B. Preparation of Uniform Si Nanoparticles for High-Performance Li-Ion Battery Anodes. *Phys. Chem. Chem. Phys.* **2016,** *18*, 1521-1525.

46. Liu, J.; Li, N.; Goodman, M. D.; Zhang, H. G.; Epstein, E. S.; Huang, B.; Pan, Z.; Kim, J.; Choi, J. H.; Huang, X.; Liu, J.; Hsia, K. J.; Dillon, S. J.; Braun, P. V. Mechanically and Chemically Robust Sandwich-Structured C@Si@C Nanotube

Array Li-Ion Battery Anodes. *ACS Nano* **2015,** *9*, 1985-1994.

47. Yang, X.; Wen, Z.; Xu, X.; Lin, B.; Huang, S. Nanosized Silicon-Based Composite Derived by *in situ* Mechanochemical Reduction for Lithium Ion Batteries. *J. Power Sources* **2007,** *164*, 880-884.

48. Chan, C. K.; Peng, H.; Liu, G.; McIlwrath, K.; Zhang, X. F.; Huggins, R. A.; Cui, Y. High-Performance Lithium Battery Anodes Using Silicon Nanowires. *Nat. Nanotechnol.* **2008,** *3*, 31-35.

49. Xu, Y.; Yin, G.; Ma, Y.; Zuo, P.; Cheng, X. Nanosized Core/Shell Silicon@Carbon Anode Material for Lithium Ion Batteries with Polyvinylidene Fluoride as Carbon Source. *J. Mater. Chem.* **2010,** *20*, 3216.

50. Xu, Y. H.; Zhu, Y. J.; Han, F. D.; Luo, C.; Wang, C. S. 3d Si/C Fiber Paper Electrodes Fabricated Using a Combined Electrospray/Electrospinning Technique for Li-Ion Batteries. *Adv. Energy Mater.* **2015,** *5*, 1400753.

51. Zhou, X.; Wu, L.; Yang, J.; Tang, J.; Xi, L.; Wang, B. Synthesis of Nano-Sized Silicon from Natural Halloysite Clay and Its High Performance as Anode for Lithium-Ion Batteries. *J. Power Sources* **2016,** *324*, 33-40.

52. Zhang, W. J. A Review of the Electrochemical Performance of Alloy Anodes for Lithium-Ion Batteries. *J. Power Sources* **2011,** *196*, 13-24.

53. Zhang, C.; Lin, Z.; Yang, Z.; Xiao, D.; Hu, P.; Xu, H.; Duan, Y.; Pang, S.; Gu, L.; Cui, G. Hierarchically Designed Germanium Microcubes with High Initial Coulombic Efficiency toward Highly Reversible Lithium Storage. *Chem. Mater.* **2015,** *27*, 2189-2194.

54. Cui, G.; Gu, L.; Kaskhedikar, N.; van Aken, P. A.; Maier, J. A Novel Germanium/Carbon Nanotubes Nanocomposite for Lithium Storage Material. *Electrochim. Acta* **2010,** *55*, 985-988.

55. Liu, N.; Wu, H.; McDowell, M. T.; Yao, Y.; Wang, C.; Cui, Y. A Yolk-Shell Design for Stabilized and Scalable Li-Ion Battery Alloy Anodes. *Nano Lett.* **2012,** *12*, 3315-3321.

56. Yoo, J. K.; Kim, J.; Lee, H.; Choi, J.; Choi, M. J.; Sim, D. M.; Jung, Y. S.; Kang, K. Porous Silicon Nanowires for Lithium Rechargeable Batteries. *Nanotechnology* **2013,** *24*, 7.

57. Minseong Ko; Sujong Chae; Sookyung Jeong; Pilgun Oh; Cho., J. Elastic a-Silicon Nanoparticles Backboned-Graphene Hybrid as a Self-Compacting Anode for High Rate Lithium-Ion Batteries. *ACS Nano* **2014,** *8*, 8591-8599.

58. Jiao, L.-S.; Liu, J.-Y.; Li, H.-Y.; Wu, T.-S.; Li, F.; Wang, H.-Y.; Niu, L. Facile Synthesis of Reduced Graphene Oxide-Porous Silicon Composite as Superior Anode Material for Lithium-Ion Battery Anodes. *J. Power Sources* **2016,** *315*, 9-15.

59. Liu, N.; Lu, Z.; Zhao, J.; McDowell, M. T.; Lee, H. W.; Zhao, W.; Cui, Y. A Pomegranate-Inspired Nanoscale Design for Large-Volume-Change Lithium Battery Anodes. *Nat. Nanotechnol.* **2014,** *9*, 187-92.

60. Barbieri, O.; Hahn, M.; Herzog, A.; Kötz, R. Capacitance Limits of High Surface Area Activated Carbons for Double Layer Capacitors. *Carbon* **2005,** *43*, 1303-1310.

61. Pognon, G.; Brousse, T.; Bélanger, D. Effect of Molecular Grafting on the Pore Size Distribution and the Double Layer Capacitance of Activated Carbon for Electrochemical Double Layer Capacitors. *Carbon* **2011,** *49*, 1340-1348.

62. Chao, D.; Zhu, C.; Yang, P.; Xia, X.; Liu, J.; Wang, J.; Fan, X.; Savilov, S. V.; Lin, J.; Fan, H. J.; Shen, Z. X. Array of Nanosheets Render Ultrafast and High-Capacity Na-Ion Storage by Tunable Pseudocapacitance. *Nat. Commun.* **2016,** *7*, 12122.

63. Chmiola, J.; Yushin, G.; Gogotsi, Y.; Portet, C.; Simon, P.; Taberna, P. L. Anomalous Increase in Carbon Capacitance at Pore Sizes Less Than 1 Nanometer. *Science* **2006,** *313*, 1760-1763.

64. Chen, Z.; Augustyn, V.; Jia, X.; Xiao, Q.; Dunn, B.; Lu, Y. High-Performance Sodium-Ion Pseudocapacitors Based on Hierarchically Porous Nanowire Composites. *ACS Nano* **2012,** *6*, 4319-4327.

65. Tian, H.; Tan, X.; Xin, F.; Wang, C.; Han, W. Micro-Sized Nano-Porous Si/C Anodes for Lithium Ion Batteries. *Nano Energy* **2015,** *11*, 490-499.

66. Ren, W.; Wang, Y.; Tan, Q.; Zhong, Z.; Su, F. Novel Silicon/Carbon Nano-Branches Synthesized by Reacting Silicon with Methyl Chloride: A High Performing Anode Material in Lithium Ion Battery. *J. Power Sources* **2016,** *332*, 88-95.

67. Zhang, C.; Pang, S.; Kong, Q.; Liu, Z.; Hu, H.; Jiang, W.; Han, P.; Wang, D.; Cui, G. An Elastic Germanium–Carbon

Nanotubes–Copper Foam Monolith as an Anode for Rechargeable Lithium Batteries. *RSC Adv.* **2013,** *3*, 1336-1340.

68. Megouda, N.; Cofininier, Y.; Szunerits, S.; Hadjersi, T.; ElKechai, O.; Boukherroub, R. Photocatalytic Activity of Silicon Nanowires under Uv and Visible Light Irradiation. *Chem. Commun.* **2011,** *47*, 991-993.

69. Qu, Y.; Zhong, X.; Li, Y.; Liao, L.; Huang, Y.; Duan, X. Photocatalytic Properties of Porous Silicon Nanowires. *J. Mater. Chem.* **2010,** *20*, 3590-3594.

70. Dai, F.; Zai, J.; Yi, R.; Gordin, M. L.; Sohn, H.; Chen, S.; Wang, D. Bottom-up Synthesis of High Surface Area Mesoporous Crystalline Silicon and Evaluation of Its Hydrogen Evolution Performance. *Nat. Commun.* **2014,** *5*, 3605.

71. Fellahi, O.; Barras, A.; Pan, G.-H.; Coffinier, Y.; Hadjersi, T.; Maamache, M.; Szunerits, S.; Boukherroub, R. Reduction of Cr(Vi) to Cr(Iii) Using Silicon Nanowire Arrays under Visible Light Irradiation. *J. Hazard. Mater.* **2016,** *304*, 441-447.

72. Stöber, W.; Fink, A.; Bohn, E. Controlled Growth of Monodisperse Silica Spheres in the Micron Size Range. *J. Colloid Interface Sci.* **1968,** *26*, 62-69.

Table of Content

3D hierarchical macro-/mesoporous silicon is synthesized through a facile scalable magnesiothermic reduction process, which shows significantly improved cyclic and rate performance with reasonable mass loading density, due to the coexistence of both macro and mesopores.